Supporting Information for

Global Crustal Thickness Revealed by Surface Waves Orbiting Mars

D. Kim[1]*, C. Duran[1], D. Giardini[1], A-C. Plesa[2], S. C. Stähler[1,3], C. Boehm[1], V. Lekic[4], S. M. McLennan[5], S. Ceylan[1], J. F. Clinton[6], P. Davis[7], A. Khan[8], B. Knapmeyer-Endrun[9], M. P. Panning[10], M. Wieczorek[11], P. Lognonné[11]

[1]Institute of Geophysics, ETH Zürich, Zürich, Switzerland; [2]DLR, Institute of Planetary Research, Berlin, Germany, Physik-[3]Institut, University of Zürich, Zürich, Switzerland; [4]Department of Geology, University of Maryland, College Park, USA; [5]Department of Geosciences, Stony Brook University, Stony Brook, USA; [6]Swiss Seismological Service, ETH Zürich, Zürich, Switzerland; [7]Department of Earth, Planetary and Space Sciences, University of California, Los Angeles, CA, USA; [8]Institute of Geochemistry and Petrology, ETH Zürich, Zürich, Switzerland; [9]Bensberg Observatory, University of Cologne, Bergisch Gladbach, Germany; [10]Jet Propulsion Laboratory, California Institute of Technology, Pasadena, CA, USA; [11]Université de Paris, Institut de Physique du Globe de Paris, CNRS, Paris, France

Contents of this file

Figures S1 to S10

Introduction

The supporting information below includes:

- Raw 10-hour SEIS data of S1222a and its spectra (Fig. S1).
- Group velocity predictions from existing 1-D models (Fig. S2).
- R2-R7 analyses focusing on narrow-bands across 20-100 s period range (Fig. S3).
- Collection of group velocity dispersion curves with two extreme model cases (Fig. S4).
- Synthetic S1222a data generated by our 3-D wavefield simulations (Fig. S5-S6).
- Depth sensitivity kernels for Rayleigh waves in VLP (Fig. S7).
- R2-R7 analysis on LP & VLP with the mantle model of KKS21 (Fig. S8).
- Thermal evolution model of Plesa et al. (2018) computed with the new crustal constraint in the main text (Fig. S9-S10).
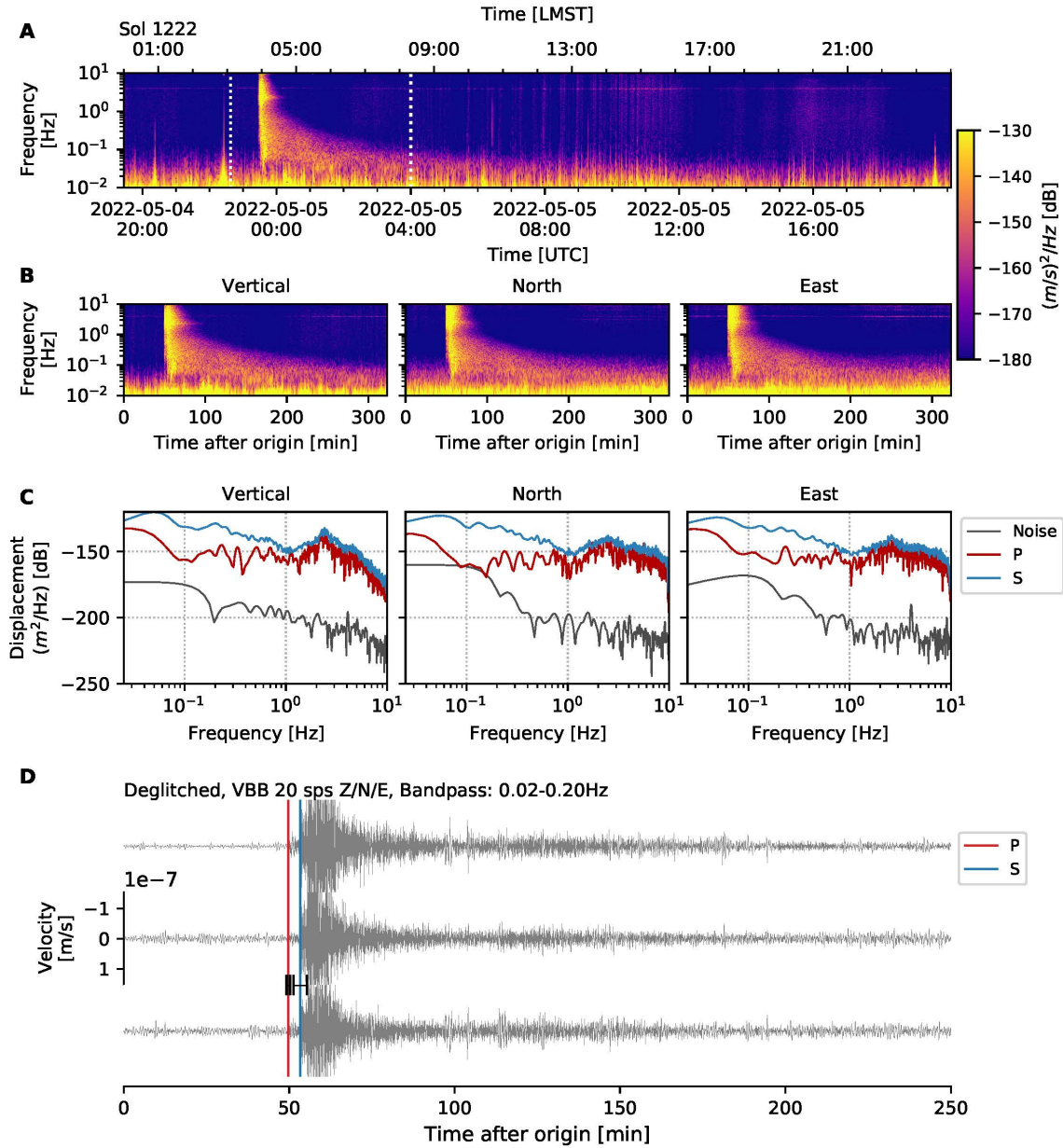
Figure S1. (**A**) One Sol long vertical-component velocity spectrogram of S1222a. (**B**) Three-component spectrograms zoomed into the event window as shown by the white dashed lines in (A). (**C**) Displacement spectra for P-, S-wave and the pre-event noise. Each spectra is computed based on the spectral time window reported by the MQS catalog. (**D**) Seismograms filtered between 0.02-0.2 Hz. Red and blue lines denote P and S arrival picks by the MQS, respectively. Uncertainties of those picks are marked by the black lines.
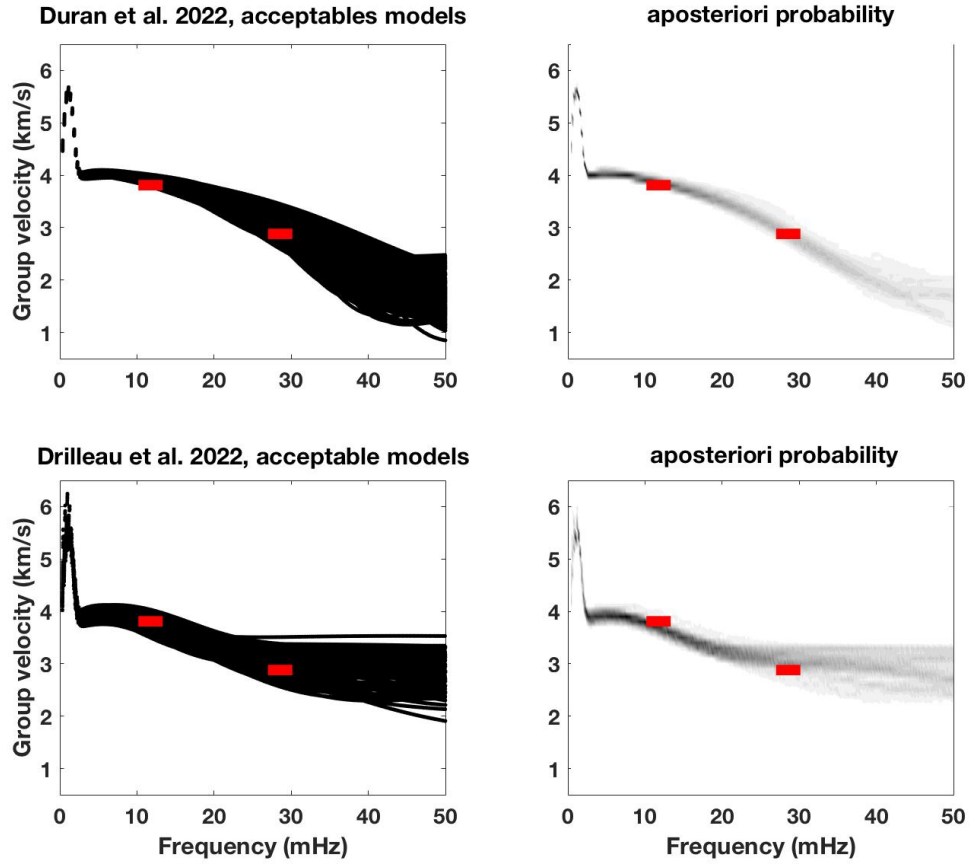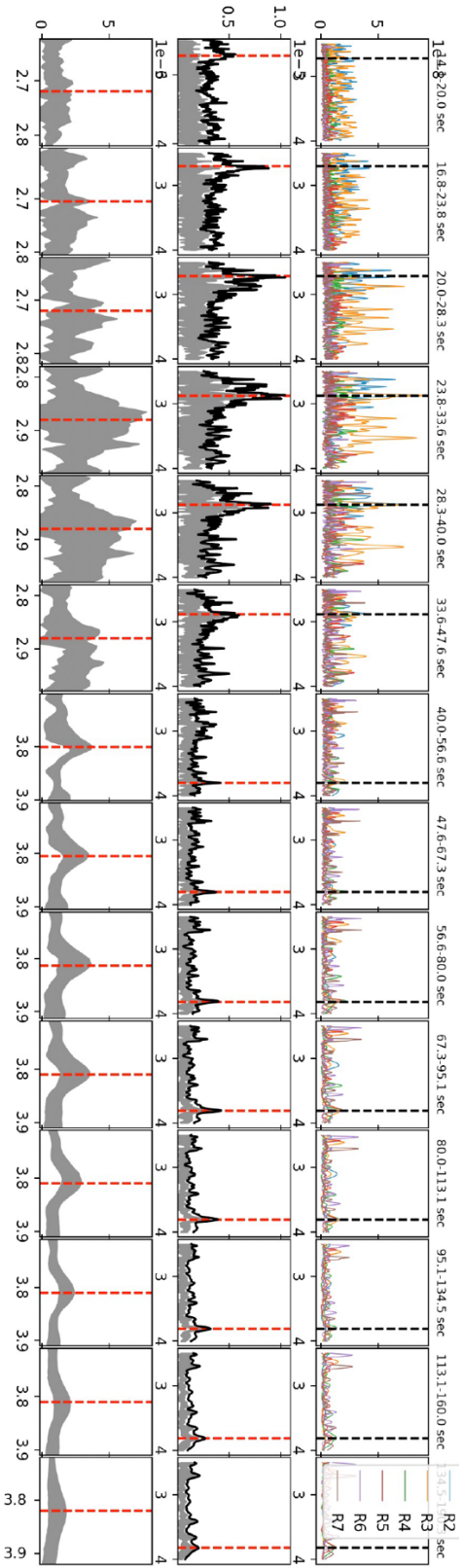
Figure S2. Group velocity predictions and their aposteriori probability made using 1000 acceptable models in Duran et al., (2022) (top row) and Drileau et al., (2022) (bottom row). Red markers denote the two distinctive group velocities observed at LP and VLP from the R2-R7 analysis discussed in the main text.
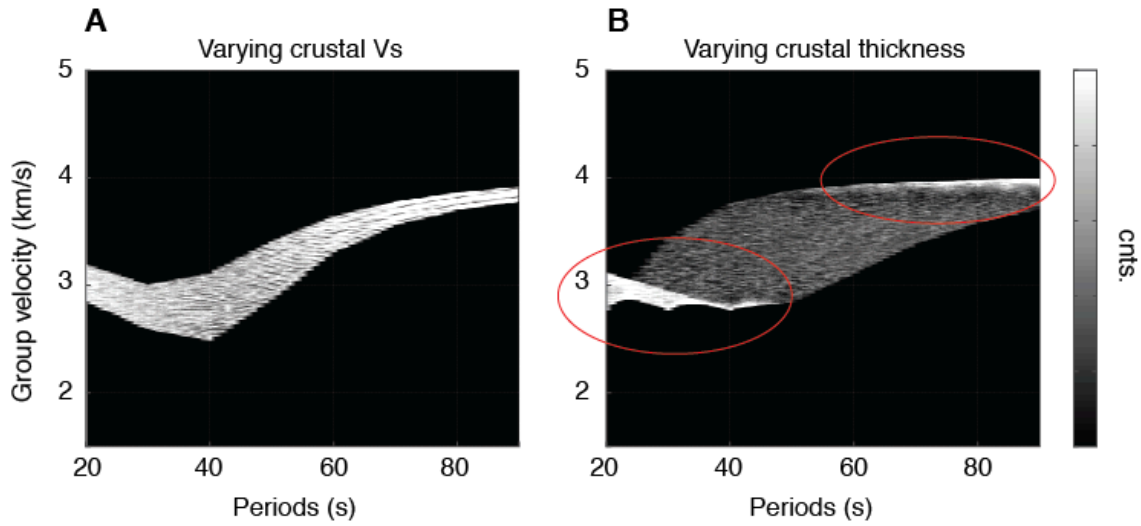
Figure S3. Individual vertical-component envelops (top row) and their 4-th root stack of the R2-R7 across different narrow period ranges between 20-100 s (middle row). Panels below show a zoom-in of those in the middle. Red dashed line denotes the largest amplitude signal in the stack.

Figure S4. Group velocity predictions shown in a form of histogram for various 1-D models randomly produced by the posterior distribution of the crustal and mantle V_s and the crustal thickness in Duran et al., (2022) and Drileau et al., (2022). Two end-member model cases are tested: (**A**) the models of varying crustal V_s with a constant crustal thickness and (**B**) the models of varying crustal thickness with a constant crustal V_s. Note that for the models considered in (B), the two distinctive group velocities dominate the predicted dispersion curves as similarly observed in Fig. 2.
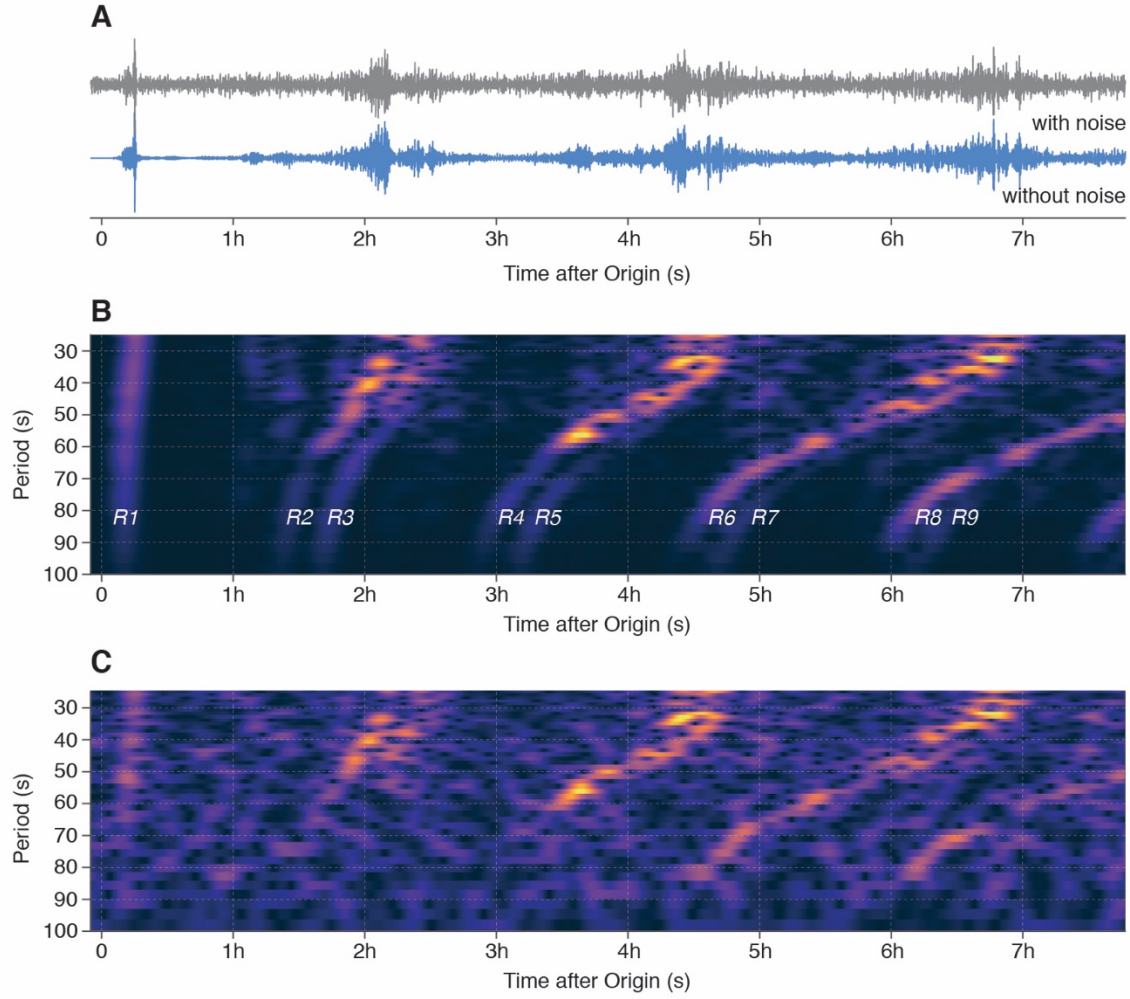
Figure S5. (**A**) 8-hour long vertical-component synthetic seismograms with and without the pre-event noise recorded in the data and (**B**-**C**) the corresponding spectrograms. 3-D wavefield simulation is performed using the 3-D crustal model overlying the mantle model of Duran et al., (2022) as discussed in the main text.
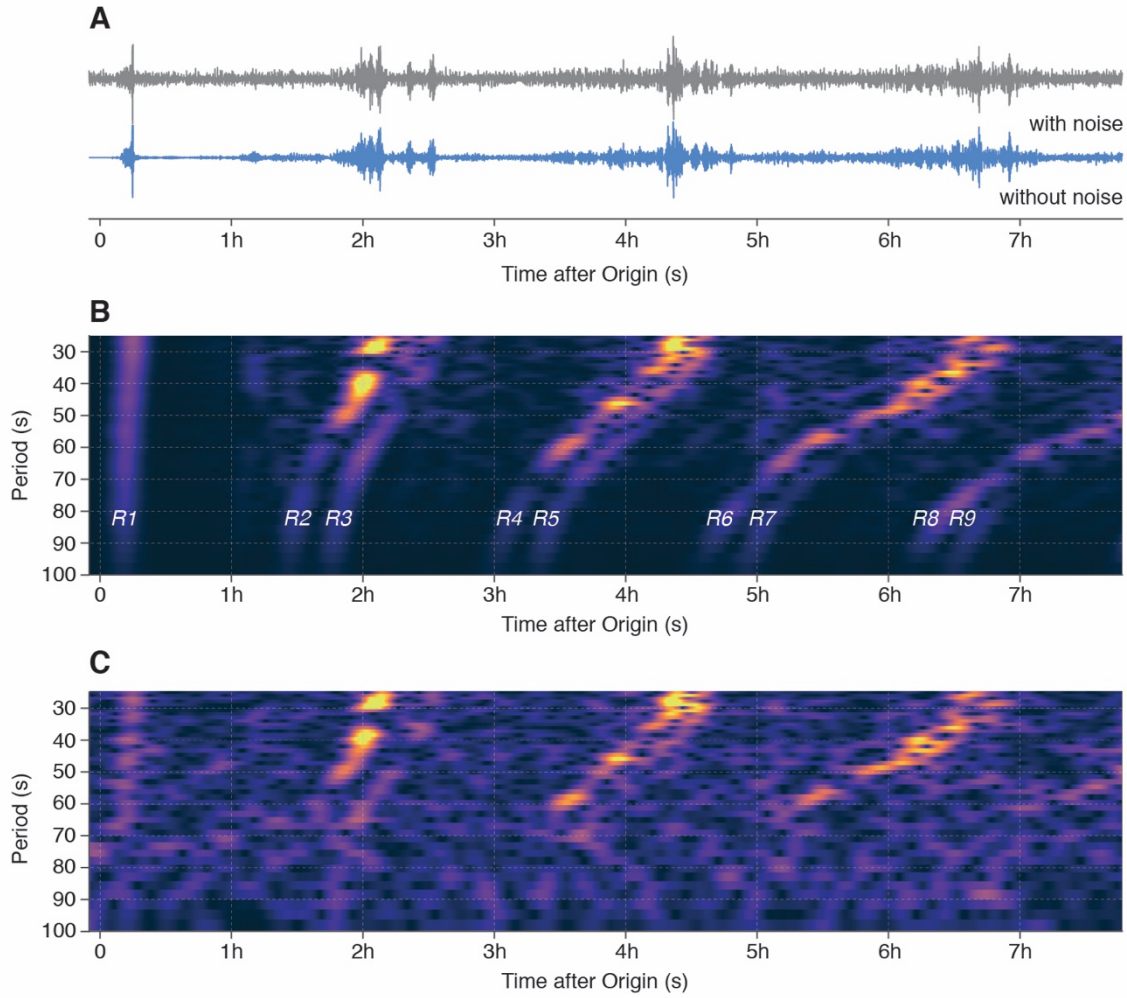
Figure S6. (**A**) 8-hour long vertical-component synthetic seismograms with and without the pre-event noise recorded in the data and (**B**-**C**) the corresponding spectrograms. 3-D wavefield simulation is performed using the 3-D crustal model overlying the mantle model of KKS21 as discussed in the main text.
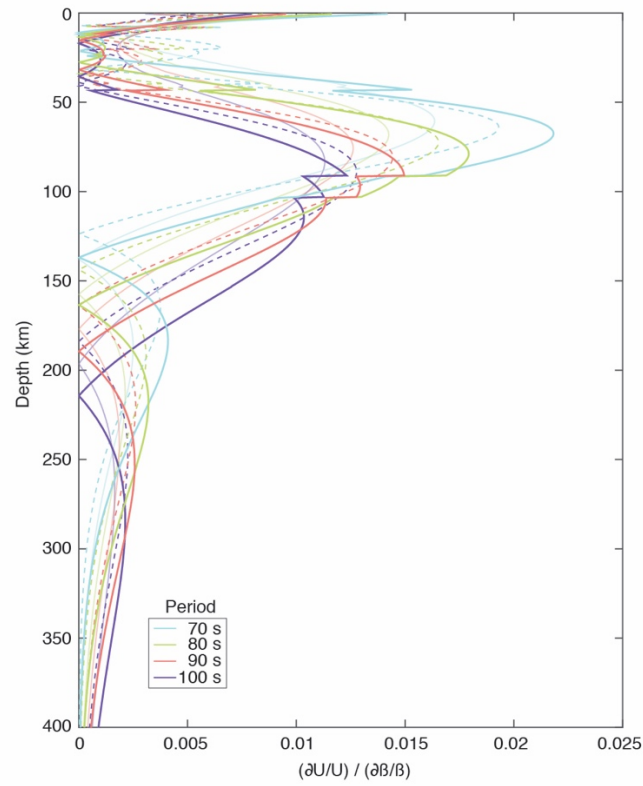
Figure S7. Depth sensitivity kernels for the fundamental mode Rayleigh waves in 70-100 s period range computed using different existing crustal velocity profiles on Mars (e.g., Knapmeyer-Endrun et al., 2021; Kim et al., 2022).
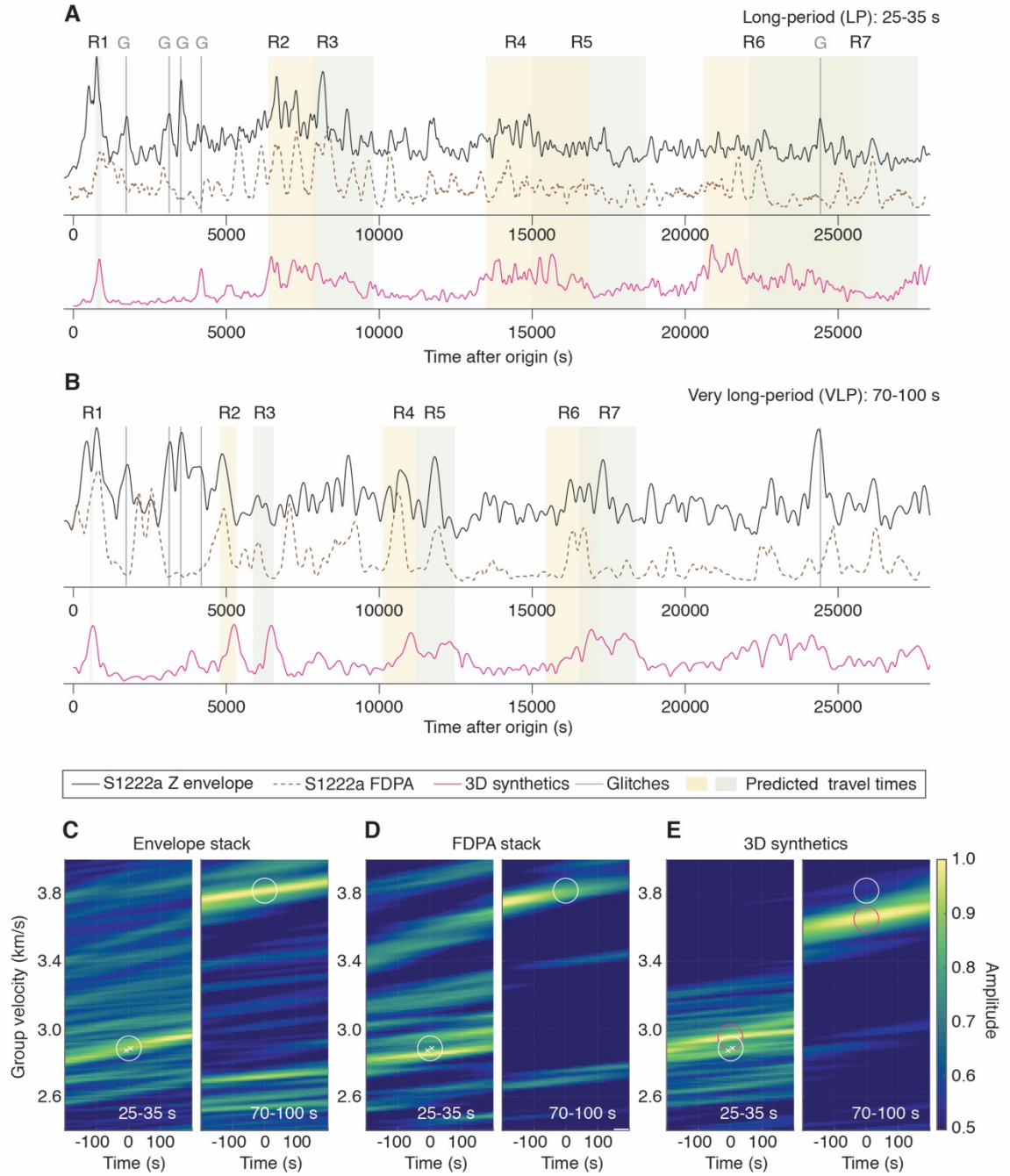
Figure S8. Same as Fig. 2 but the synthetic stack in (E) is based on the 3-D crustal model overlying the mantle model of KKS21(e.g., Fig. S6).
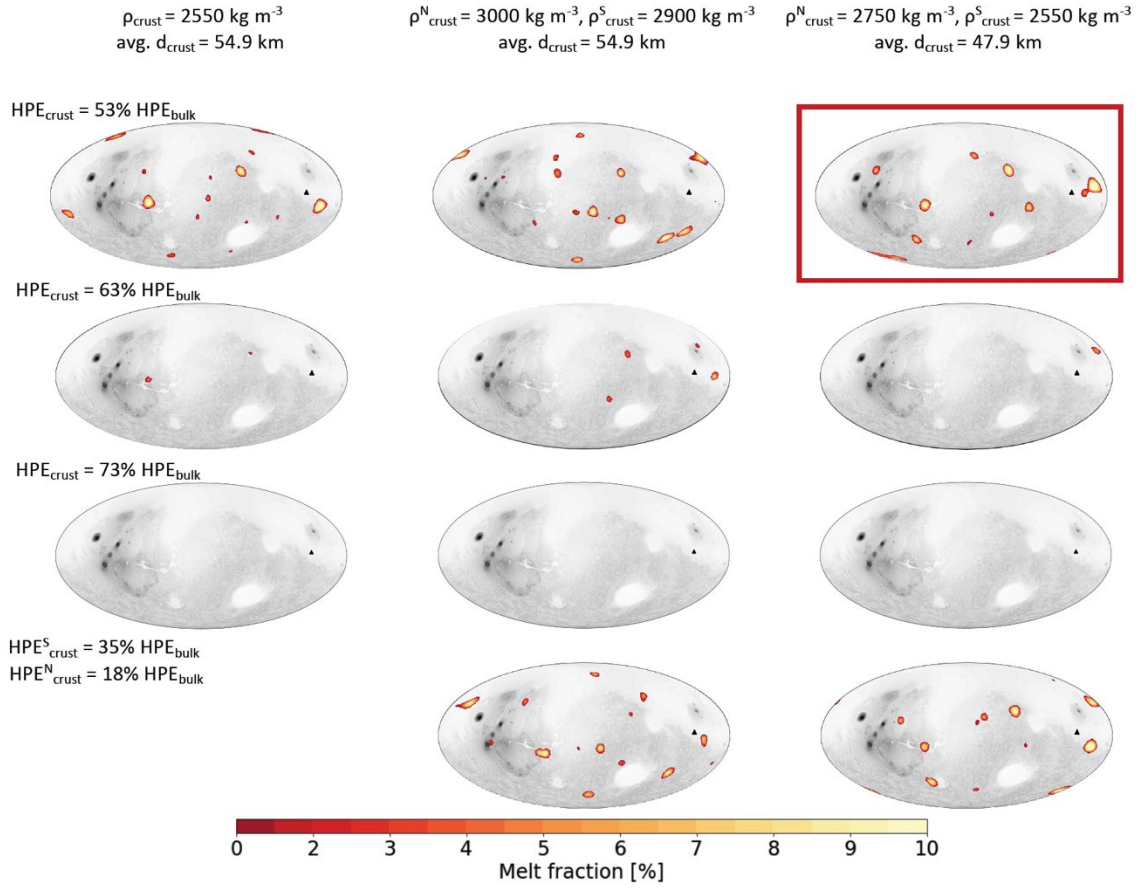
Figure S9. Distribution of partial melt produced by mantle plumes in the interior of Mars at present day. The left column shows the constant density models that employ an average crustal thickness of 55 km and contain 53%, 63%, and 73% of the total bulk content of radioelements in the crust. The middle and right column models have a small density difference of 100 kg/m^3 and 200 kg/m^3 between northern lowlands vs. southern highlands with an average crustal thickness of 55 km and 48 km, respectively. The mantle parameters are chosen as in Plesa et al., (2022). Best-fitting model is outlined in red which favors mantle plumes that can produce melt up to the present day in and around Cerberus Fossae.

ρ_{crust} = 2550 kg m^{-3}
avg. d$_{crust}$ = 54.9 km

ρ^N_{crust} = 3000 kg m^{-3}, ρ^S_{crust} = 2900 kg m^{-3}
avg. d$_{crust}$ = 54.9 km

ρ^N_{crust} = 2750 kg m^{-3}, ρ^S_{crust} = 2550 kg m^{-3}
avg. d$_{crust}$ = 47.9 km

HPE$_{crust}$ = 53% HPE$_{bulk}$

HPE$_{crust}$ = 63% HPE$_{bulk}$

HPE$_{crust}$ = 73% HPE$_{bulk}$

HPE$^S_{crust}$ = 35% HPE$_{bulk}$
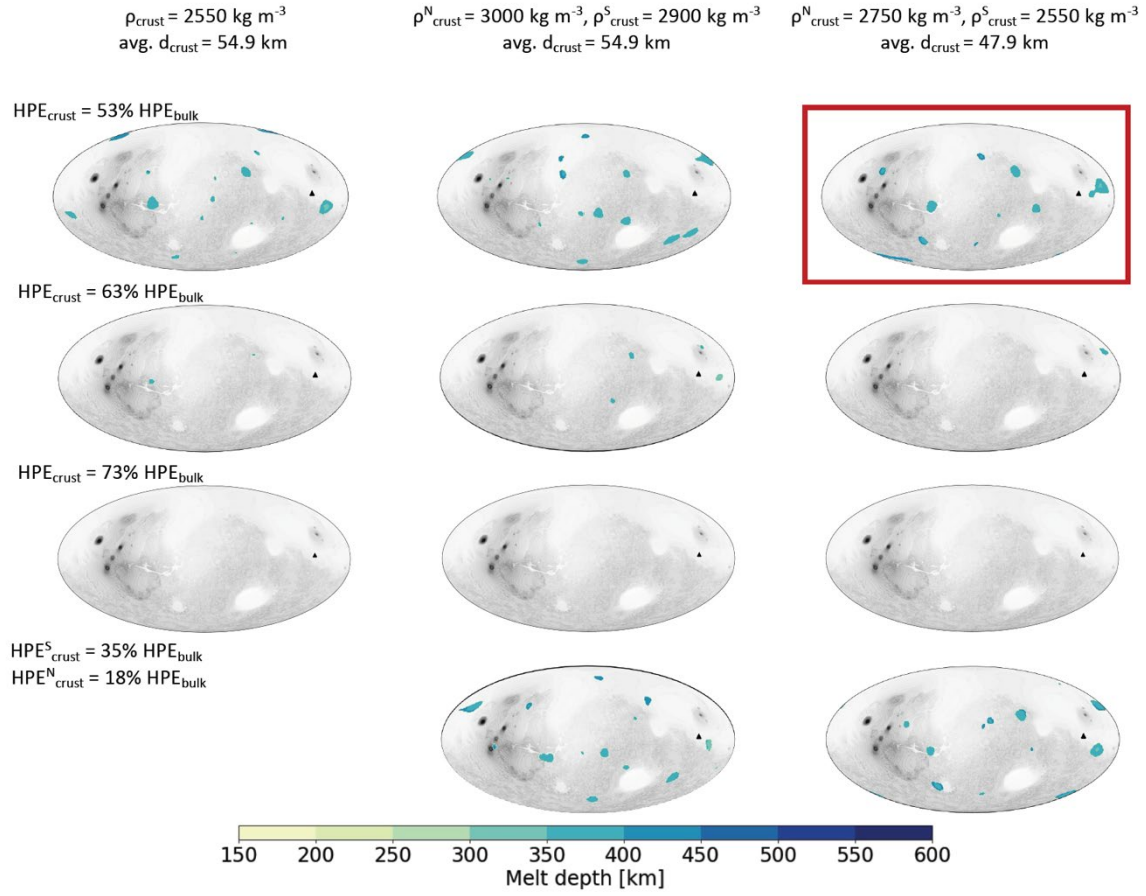HPE$^N_{crust}$ = 18% HPE$_{bulk}$

Melt depth [km]

Figure S10. Distribution of the corresponding melt depth based on the models shown in Fig. S9. Best-fitting model is outlined in red which favors mantle plumes that can produce melt up to the present day in and around Cerberus Fossae.